Discover Applied Sciences

Research

Hemodynamic characterization of abdominal aortic fusiform aneurysm: insights from computational fluid dynamics simulations

Talaat Abdelhamid[1,2] · **Ahmed G. Rahma**[3]

Received: 11 January 2024 / Accepted: 23 May 2024
Published online: 13 November 2025

Abstract
This numerical study consists of two different phases. In phase I, the blood flow is numerically simulated in a pipe with a diameter of 3.5 mm and a length of 61.6 mm with a vascular dilation (*d/D*) range from 1 to 2.6 (0–160%) where *d* is the dilation diameter and *D* is the straight cylindrical vessel diameter. In phase II, the simulations are performed on two models built based on the computed tomography angiography of the actual case of a patient-specific abdominal aorta fusiform aneurysm and a healthy case of the abdominal aorta. This numerical study aims to investigate the blood flow behavior and wall shear stress distribution in vascular dilations, focusing specifically on abdominal aortic aneurysm cases. Computational fluid dynamics simulations are performed on benchmark geometries and two computed tomography angiography-based models of abdominal aortic, one from a 54-year-old woman with abdominal aortic aneurysm and another from a healthy 43-year-old woman. The simulations utilize Ansys Fluent package software with boundary conditions obtained from patient data via ultrasonography. The results reveal distinct flow regimes in vascular dilations, including stable flow, critical flow, transient flow, and stable flow with recirculation. In abdominal aortic aneurysm cases, reduced blood velocity and complex flow patterns with recirculation zones are observed within the aneurysm zone. Wall shear stress distribution varies throughout the cardiac cycle, with higher values during systole and at bifurcations, highlighting the importance of fluid-wall interactions.

Keywords Hemodynamics · Abdominal aortic aneurysm · Computational fluid dynamics · Flow recirculation · Flow regimes · Wall shear stress

1 Introduction

Hemodynamic analyses of the vascular system in patients have proven to be of significant value in understanding and treating associated diseases [1, 2]. These analyses play a crucial role in assessing conditions such as vascular system stenosis [3, 4], aneurysms [5] including fusiform types [6, 7] and saccular types [8, 9] as well as false and dissection types [10]. Computational fluid dynamics is a robust tool employed to investigate various hemodynamic wall parameters, including wall pressure, and wall shear stress, along with analyzing blood flow behavior such as flow structure and flow vortex [11–13]. Xiang et al. [14] conducted a study on the influence of hemodynamics on the rupture of saccular intracranial aneurysms. The findings demonstrated that computational fluid dynamics simulations have the capability to accurately assess the risk of intracranial aneurysms, provided an actual database is available [8, 15]. Moreover, it serves as

✉ Talaat Abdelhamid, Talaat_abdelhamid@el-eng.menofia.edu.eg; talaat.abdelhamid@unimi.it | [1]Physics and Mathematical Engineering Department, Faculty of Electronic Engineering, Menoufiya University, Menouf 32952, Egypt. [2]Dipartimento di Matematica, Università degli Studi di Milano, 20133 Milan, Italy. [3]Université de Strasbourg, CNRS ICUBE UMR 7357, 67000 Strasbourg, France.

an invaluable tool for comprehending vascular disorders both prior to and following treatment [16, 17]. Wang et al. [18], numerically examined the thrombosis risk associated with fusiform coronary artery aneurysms. The findings suggested that the risk of thrombosis is influenced not only by the diameter of fusiform coronary artery aneurysms but also by the wall parameters. As a result, numerical simulations were conducted on various diameters of fusiform coronary artery aneurysms to investigate their impact on hemodynamic parameters. The results demonstrated a decrease in the wall shear stress as the aneurysm diameter increased.

The abdominal aortic aneurysm is characterized by the dilation of the lower portion of the vessel due to weakness in the arterial wall. The prevalence of the aneurysm cases varies from 0.5 to 6.0% of the global population [19–21]. In general, the aneurysm typically leads to a 50% increase in vessel diameter when compared to that of a healthy abdominal aorta [22]. Salman et al. [23] proposed a computational fluid dynamic procedure and experimental setup to explore the underlying causes of aneurysm rupture. Through computational and experimental investigations, the study revealed that several parameters, including wall shear stress, flow recirculation, and wall pressure, have a significant impact on the aneurysm rupture. Scotti et al. [24] employed numerical simulations to investigate the impact of aneurysm and wall thickness on blood flow patterns and wall hemodynamic parameters. The abdominal aortic aneurysm was created using five idealized fusiform aneurysm ratios. The presence of an aneurysm with asymmetric regional variations was found to increase the risk of rupture and result in higher mechanical stress compared to symmetric fusiform aneurysms. As the aneurysm ratio increased about 0.2, a flow vortex appeared, generating recirculation that moved towards the proximal end of the aneurysm.

In the field of cardiovascular computational fluid dynamics, both benchmark models and Computed Tomography Angiography (CTA)-based models are commonly employed [1, 25]. These models serve as essential tools for studying and analyzing the hemodynamics of the cardiovascular system. By utilizing these approaches, researchers gain valuable insights into the flow behavior, pressure distribution, and other hemodynamic parameters, contributing to a better understanding of cardiovascular diseases and their treatments. In Algabri study [26], a three-dimensional simulation was conducted to analyze the blood flow patterns in angular neck abdominal aortic aneurysms. Simplified computational domains were created based on a patient-specific abdominal aortic aneurysm with a variable angular neck. The simulation was performed under steady-state conditions using the commercial software package ANSYS FLUENT. The findings revealed that an increase in the aorta neck angle resulted in a decrease in the flow vortex within the aneurysm. Furthermore, regions of higher velocity were observed near the middle of the aorta, particularly in the contours of velocity streamlines. Petuchova [27] conducted a comprehensive study utilizing simulations to investigate the hemodynamic characteristics of ascending aortic aneurysms compared to healthy cases. The research involved constructing vascular system models based on CTA data, with one model representing a healthy individual and the other representing a patient with an ascending aortic aneurysm. The simulations provided valuable insights into various parameters, including maximum velocity and wall shear stress, allowing for a detailed comparison between the two cases. The blood can be described as an incompressible Non-Newtonian fluid [28, 29].

This paper aims to study the flow patterns and hemodynamics of aortic abdominal fusiform aneurysms through numerical simulations, providing insights into their fluid behavior: Section 3 provides a problem description and introduces the system of incompressible Navier-Stokes equations, which are discretized using a fully implicit finite element method. The validation of the numerical approach is also discussed in relation to existing literature. In Section 3, the numerical simulations are performed using Ansys Fluent to analyze various flow parameters, including wall shear stress, wall pressure, and flow recirculation. The simulations are conducted on simplified benchmark geometries of abdominal aortic aneurysm. Additionally, a realistic abdominal aortic aneurysm geometry reconstructed from CTA data is considered and compared to an CTA-based model of a healthy abdominal aorta. Finally, Section 4 concludes with some key remarks.

2 Numerical methods

2.1 Problem identification

The numerical simulations in this paper consist of two different phases. In phase I, the blood flow is numerically simulated in a pipe with a diameter of 3.5 mm and 61.6 mm as a length with a vascular dilation (d/D) range from 1 to 2.6 (0–160%) where d is the dilation diameter and D is the straight cylindrical vessel diameter as it is shown in Fig. 1. These simplified models are called benchmarks. In phase II, the simulations are performed on two models built based on the

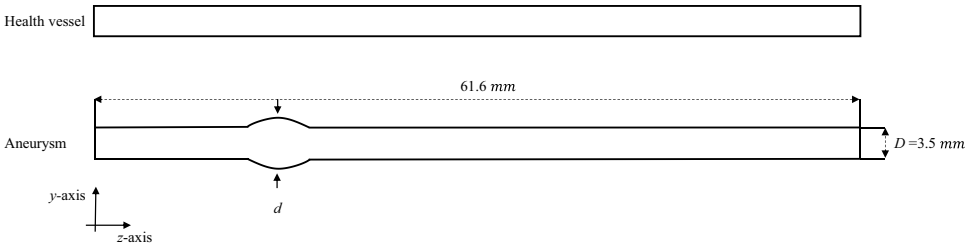

Fig. 1 Schematic diagram of the benchmark computational domain

CTA of the actual case of a patient-specific abdominal aorta fusiform aneurysm and a healthy case of the abdominal aorta, as shown in Fig. 10.

2.2 Governing equations and boundary conditions

The blood motion governed by Navier–Stokes equations in the laminar flow condition is definedas in [30]:

Continuity Equation (Mass Conservation):

$$\nabla \cdot \vec{u} = 0 \tag{1}$$

Momentum Conservation:

$$\rho\left(\frac{\partial \vec{u}}{\partial t} + \vec{u} \cdot \nabla \vec{u}\right) = -\nabla p + \nabla \cdot \tau + \rho \vec{g} \tag{2}$$

The stress tensor (τ) can be represented as follows:

$$\tau = \begin{bmatrix} \tau_{xx} & \tau_{xy} & \tau_{xz} \\ \tau_{yx} & \tau_{yy} & \tau_{yz} \\ \tau_{zx} & \tau_{zy} & \tau_{zz} \end{bmatrix} \tag{3}$$

where u, v, and w are the blood flow velocities in x, y, and z coordinates, respectively. It is assumed that blood can be described as an incompressible Non-Newtonian fluid with a four-parameter viscosity model (Carreau model), blood density ρ of 1063 kg/m^3, and g is the constant gravitational acceleration. In our work, the body force was neglected (g = 0 m/s^2). The wall of the blood vessels is assumed to be rigid with no slipping ratio, as described in Table 1 for the blood properties and carreau model [31, 32]. The carreau fluid model is a four-parameter law that describes the behavior of fluids. At low shear rates, carreau fluids behave as Newtonian fluids, while at high shear rates, they behave as Non-Newtonian fluids that follow the power-law fluid behavior. Therefore, the carreau model is recommended for simulating blood flow in arteries and achieving accurate predictions [33]. The equations for the carreau model can be expressed as in [34], where:

$$\mu(\dot{\gamma}) = \mu_{\infty} + \left(\mu_0 - \mu_{\infty}\right)\left[1 + (\lambda\dot{\gamma})^2\right]^{\left(\frac{n-1}{2}\right)} \tag{4}$$

The model equation incorporates several parameters: μ_{∞} (=0.035), which represents the infinite viscosity of blood; μ_0 (=0.436), the viscosity at zero shear rates; λ (=3.3), the characteristic time of the fluid; and

n (=0.36), the power-law index, and $\dot{\gamma}$ is the shear rate (s^{-1}).

Table 1 Blood flow properties used for phase I, (Luo et al. [1])

Properties	Value	Unit
Blood density ρ	1063	kg/m^3
Entrance velocity v_{in}	10.525	cm/s
Outlet pressure P	11,999 (90 mmHg)	Pa

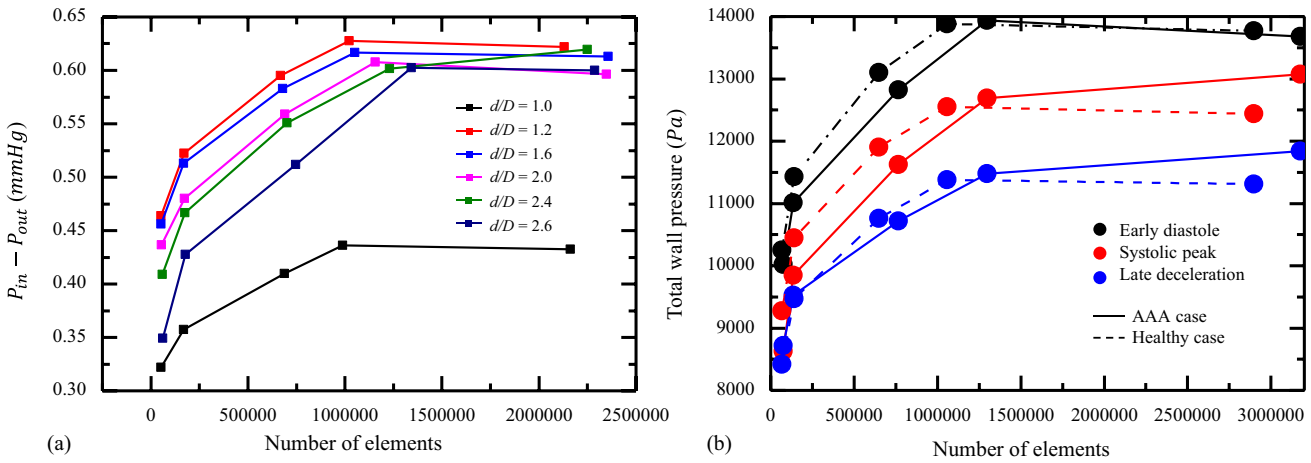

Fig. 2 Mesh independence study for **a** the benchmarks, and **b** the CTA-Based models

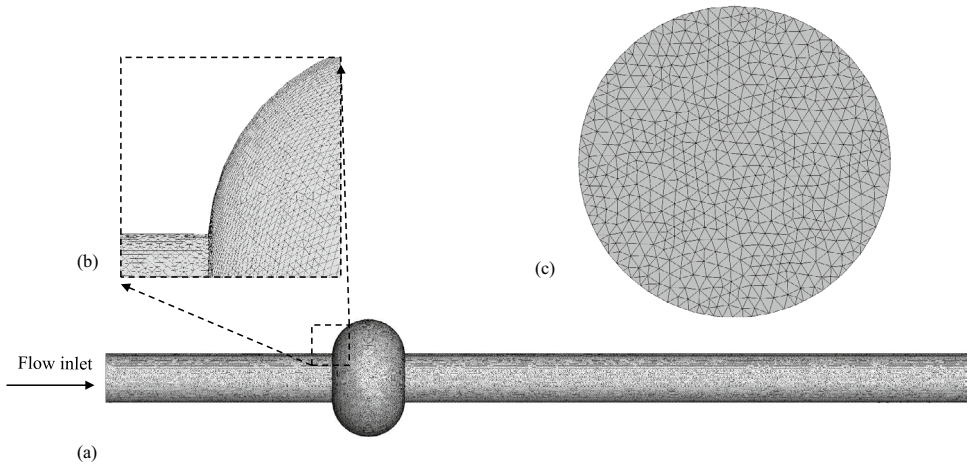

Fig. 3 **a** The mesh details for the benchmark, **b** Zoomed-in view of the meshing for the idealized fusiform aneurysms, and **c** Inlet zoomed-in view

The simulations conducted in this study aim to solve the system governing laminar flow within a three-dimensional computational domain, focusing on Reynolds numbers (*Re*) below 2300. To ensure accurate results, second-order upwind schemes are employed for all conservation equations. The coupling of pressure and velocity fields is achieved through a coupled scheme, where the momentum equations and pressure-based continuity equations are solved simultaneously. This integrated approach facilitates a comprehensive analysis of the flow behavior. In order to achieve convergence, a pseudo-transient scheme is implemented, utilizing a pseudo-transient coefficient of 0.7 for fluid zones and 1.0 for solid zones. This scheme is particularly effective in ensuring strong convergence, which is crucial for capturing the intricate dynamics of blood flow. By gradually transitioning towards a steady state, the pseudo-transient scheme enables the solution to reach a robust and reliable state, providing valuable insights into the complex flow characteristics.

2.3 The computational grids and time-step

2.3.1 Mesh independence study

To ensure accurate computational results, a mesh independence study is conducted to generate a suitable meshing, as shown in Figs. 2 and 3.

I. Benchmarks

Table 2 shows different Meshes (Mesh 1, Mesh 2, Mesh 3, Mesh 4, and Mesh 5) at different dilation ratios *d/D* (= 1.0, 1.2, 1.6, 2, 2.4, and 2.6). These grid sizes were chosen to ensure an accurate representation of the flow phenomena

Table 2 Grid sizes for different dilation ratios of the benchmark

Dilation Ratio (d/D)	Mesh 1	Mesh 2	Mesh 3	Mesh 4	Mesh 5
1	51,476	168,478	687,942	987,648	2,561,458
1.2	52,489	171,456	668,941	1,021,949	2,129,887
1.6	52,798	169,875	678,941	1,051,678	2,356,987
2	54,689	172,469	689,745	1,156,945	2,347,954
2.4	58,976	175,489	701,598	1,232,550	2,249,761
2.6	61,357	178,456	746,984	1,341,626	2,287,941

and behavior within the benchmarks at different dilation ratios, as shown in Table 2. Overall, the findings of the mesh independence study indicate that using Mesh 4 strikes a suitable balance between accuracy and computational efficiency for the simulations. Figure 2a illustrates the relationship between the pressure difference and the number of elements in different meshing systems. The results reveal that there is no significant impact on the pressure difference when the number of elements exceeds 987,648 for the benchmarks with $d/D = 1$, $N = 1{,}021{,}949$ for $d/D = 1.2$, $N = 1{,}051{,}678$ for $d/D = 1.6$, $N = 1{,}156{,}945$ for $d/D = 2$, $N = 1{,}232{,}550$ for $d/D = 2.4$, and $N = 1{,}341{,}626$ for $d/D = 2.6$.

II. CTA-based models

The CTA-based models were simulated using different grid sizes. For the aneurysm case, the grids consisted of 76,145, 135,987, 765,148, 1,298,197, and 3,175,761 elements. The healthy model was simulated with grids containing 68,745, 140,568, 648,954, 1,058,792, and 2,897,456 elements. Figure 2b illustrates the relationship between the total wall pressure and the number of elements in the different meshing systems. The results indicate that there is no significant impact on the wall total pressure when the number of elements exceeds 1,298,197 for an aneurysm case at 1,058,792 elements for the healthy model. Accordingly, the fourth mesh was selected in the current numerical simulation for both models.

2.3.2 Time-step independence study

A comprehensive time-step Δt independence study was performed on the CTA-Based models to examine the influence of varying the time step on the total wall pressure. The four values of Δt is selected, 0.001s, 0.005s, 0.01s, and 0.1s, respectively. The results demonstrated that the total wall pressure remained relatively unchanged at $\Delta t > 0.005$, for both aneurysm and healthy cases, indicating that further decreasing the time step did not significantly affect the total wall pressure. This observation is depicted in Fig. 4. Overall, the findings of the study suggest that utilizing a time step of $\Delta t = 0.005$ provides a suitable balance between accuracy and computational efficiency for the simulations.

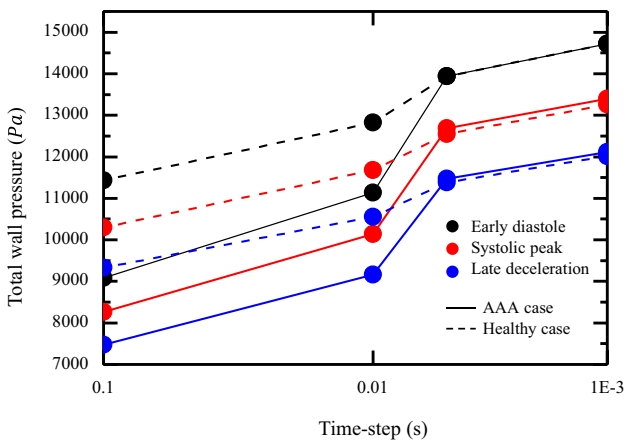

Fig. 4 Time-step independence study for the CTA-based models

3 Results and discussion

3.1 Phase I: the simplified abdominal aorta fusiform aneurysms benchmark

A comprehensive investigation of the hemodynamic parameters is introduced using a steady simulation with the boundary conditions presented in Table 1.

3.1.1 The flow structures

The presence of the aneurysm has a significant impact on the appearance of the flow recirculation and the behavior of the flow. In Figs. 5 and 6, four regimes of flow can be observed. Regime 1 occurs at small values of *d/D* where $1 \leq d/D < 1.4$. This regime represents stable flow without the appearance of flow recirculation. Moving to Regime 2, identified as the critical flow regime, we observe flow behavior for $1.4 \leq d/D < 1.8$. In this regime, there is an uneven distribution of flow recirculation along the z-axis of the aneurysm. This uneven distribution arises from flow interaction and separation at the edges of the aneurysm, which increases the risk of vascular vessel rupture (see Figs. 7 and 8). Transitioning to Regime 3, also known as the transient flow regime, we consider $1.8 \leq d/D < 2.2$. This regime represents a transitional state between the critical flow regime (Regime 2) and the stable reticulation flow regime (Regime 4). Finally, in Regime 4, characterized as the stable reticulation flow regime, we have $d/D \geq 2.2$ but less or equal to 2.6. In this regime, an even flow recirculation along the z-axis of the aneurysm is observed. The formation of a pillow-like structure prevents flow interaction with the edges of the aneurysm, resulting in decreased hemodynamic wall parameters (see Figs. 7 and 8). These flow regimes highlight the complex and dynamic nature of flow behavior within aneurysms, emphasizing the significance of considering the aneurysm diameter-to-vessel diameter ratio in understanding the hemodynamic characteristics and potential risks associated with aneurysm development.

3.1.2 The pressure variation

The effect of the vasodilation ratio (*d/D*) on the artery pressure drop is illustrated in Fig. 7. It is observed that increasing the vasodilation ratio leads to a higher pressure drop across the vessel dilation, indicating an increased flow energy loss through the aneurysm. In the first regime and at the beginning of the second regime, the pressure drop rises as the *d/D* ratio increases. However, as the transition from the critical regime to the transient regime occurs, the pressure drop starts to decrease. Ultimately, in the stable reticulation flow regime, the pressure drop stabilizes at an approximately constant level. These findings demonstrate the significant impact of the vasodilation ratio on the flow characteristics and energy dissipation in the aneurysm.

Figure 8 presents the wall pressure distribution along the benchmarks. It is observed that the wall pressure exhibits a homogenous decrease both before and after the dilation. Within the dilation section, a sudden decrease in wall

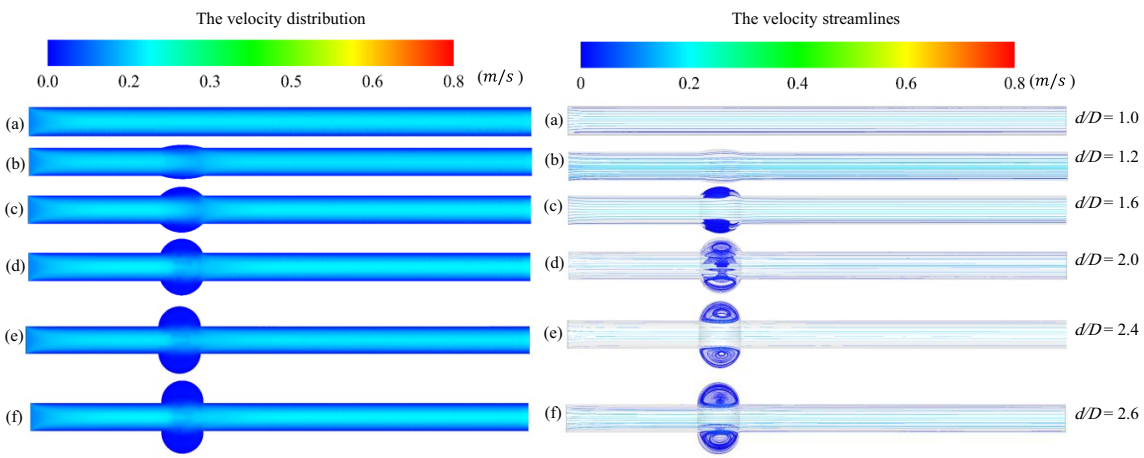

Fig. 5 The distribution of the velocity (Left) and the velocity streamlines (Right) at variable d/D

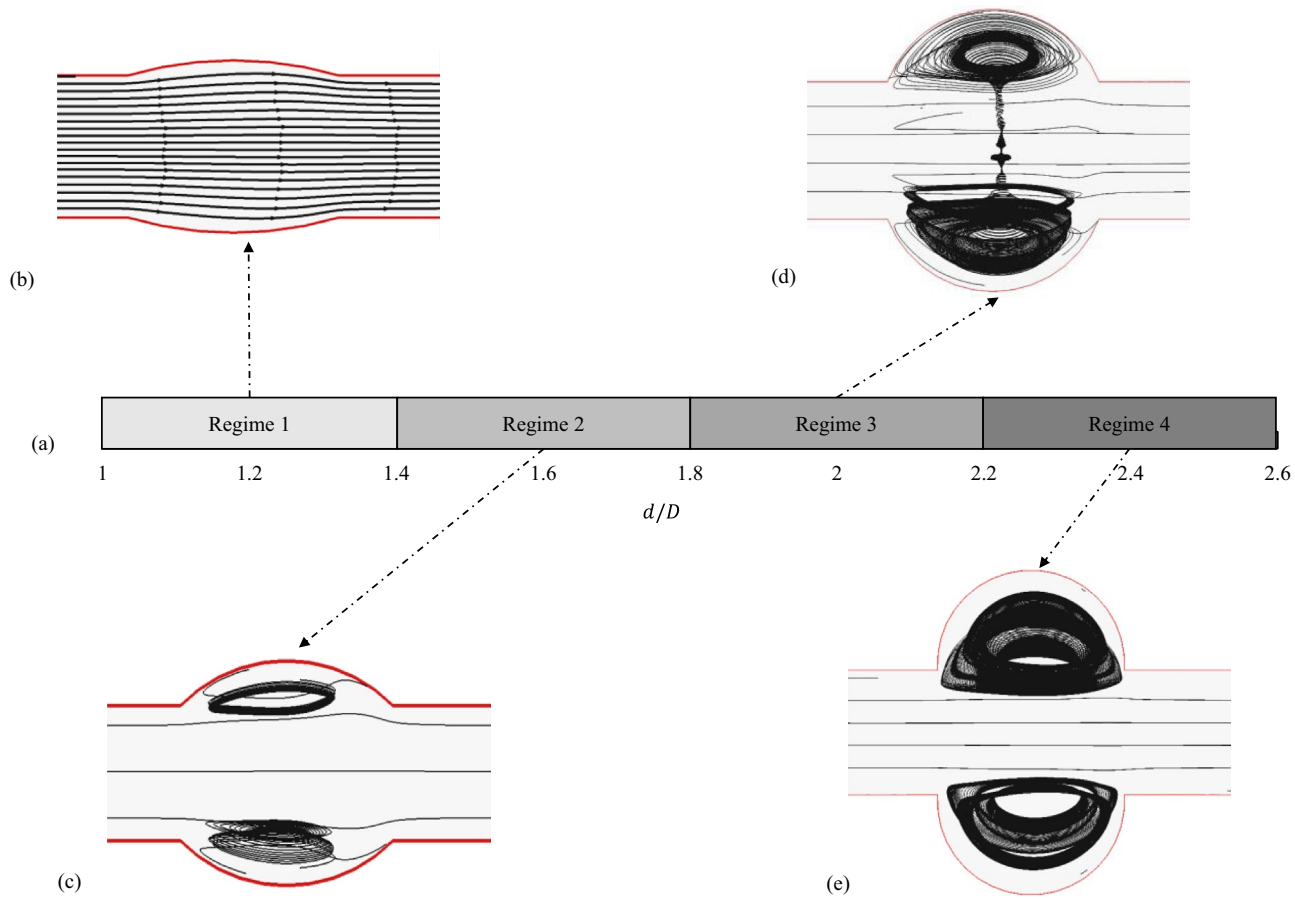

Fig. 6 **a** Flow pattern map of the flow regimes due to the change of d/D, **b** Regime 1: stable flow without flow recirculation, **c** Regime 2: Critical flow, **d** Regime 3: Transient flow, and **e** Regime 4: stable reticulation flow

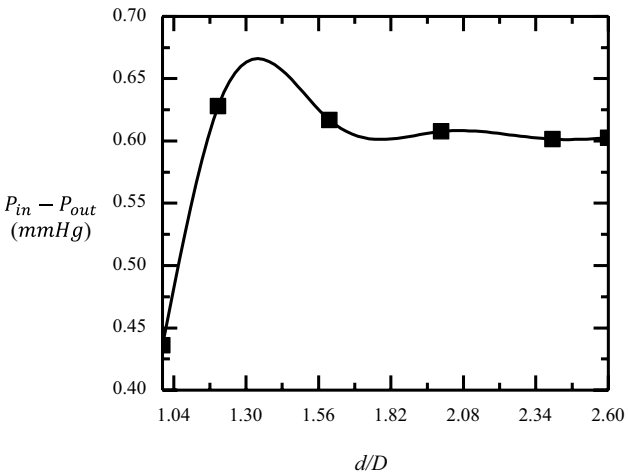

Fig. 7 The pressure between the output and the input of the fusiform aneurysm benchmarks at different d/D

pressure is observed at the beginning of the dilation, followed by an increase along the z-axis of the aneurysm, as depicted in Fig. 8g. This increase in wall pressure is attributed to flow separation at the edges of the dilation. Notably, the wall pressure values are significantly higher in the critical flow regime compared to the other flow regimes. These findings highlight the complex behavior of wall pressure and its variation along the aneurysm, particularly in the dilation region.

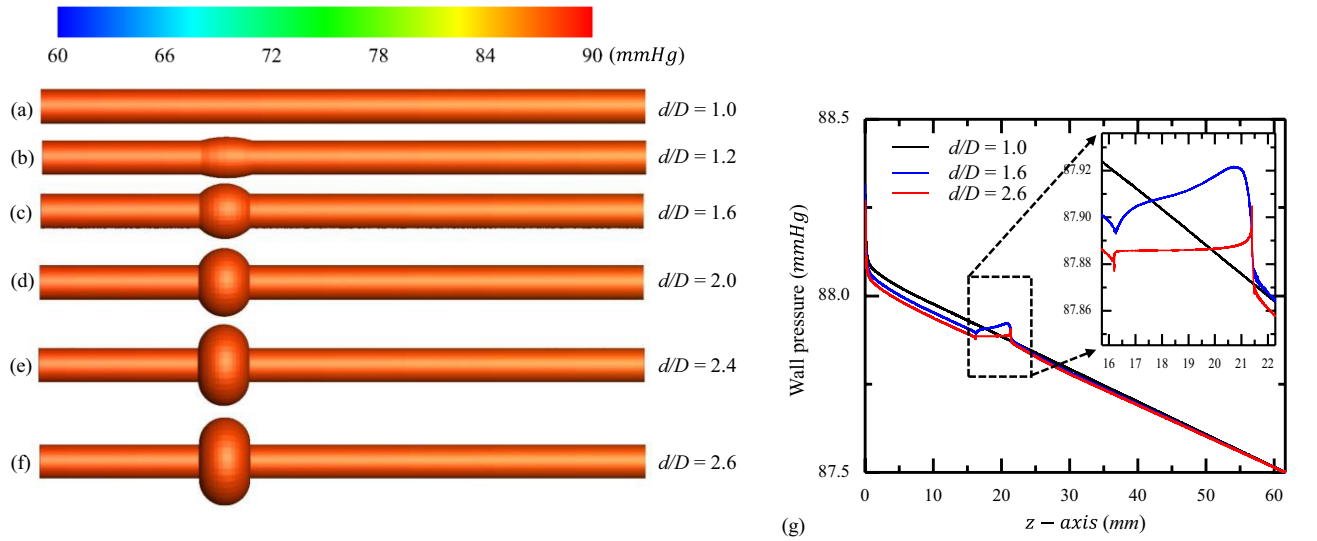

Fig. 8 **a–f** The distribution of the wall pressure, and **g** wall pressure profile along z-axis of the benchmarks at different d/D

3.1.3 The wall shear stress

Figure 9 presents the investigation of wall shear stress around the vascular dilation. The distribution of wall shear stress exhibits a qualitative similarity to the wall pressure distribution shown in Fig. 8. Along the z-direction, the wall shear stress generally decreases, except at the end zone of the dilation. At the beginning of the dilation, there is a sudden decrease in wall shear stress, indicating reduced flow contact with the vessel wall. Moreover, a significant increase in wall shear stress is observed at the end of the aneurysm zone, attributed to flow separation at the edges where the flow contacts the edges. Notably, the wall shear stress reaches its maximum value in Regime 2 compared to Regimes 3 and 4. In the stable recirculation flow regime, there is a sudden decrease in wall shear stress (Compared to Regime 2) at the end of the dilation due to the formation of a pillow, which reduces flow interaction with the bulge outlet edge.

3.2 Phase II: CTA-based models

Unsteady computational fluid dynamics simulations are performed on realistic models of actual abdominal aortic aneurysm for a 54-year-old woman and a healthy case of a 43-year-old woman. The models are constructed from CTA images

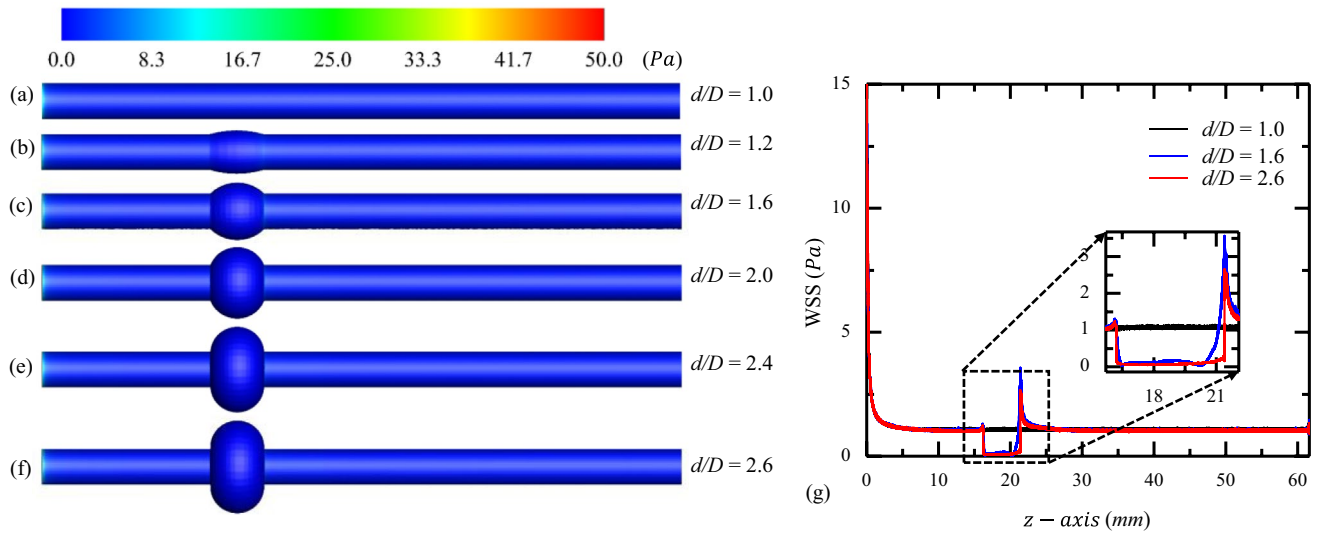

Fig. 9 **a–f** The distribution of wall shear stress, and **g** wall shear stress profile along z-axis for the benchmarks at different d/D

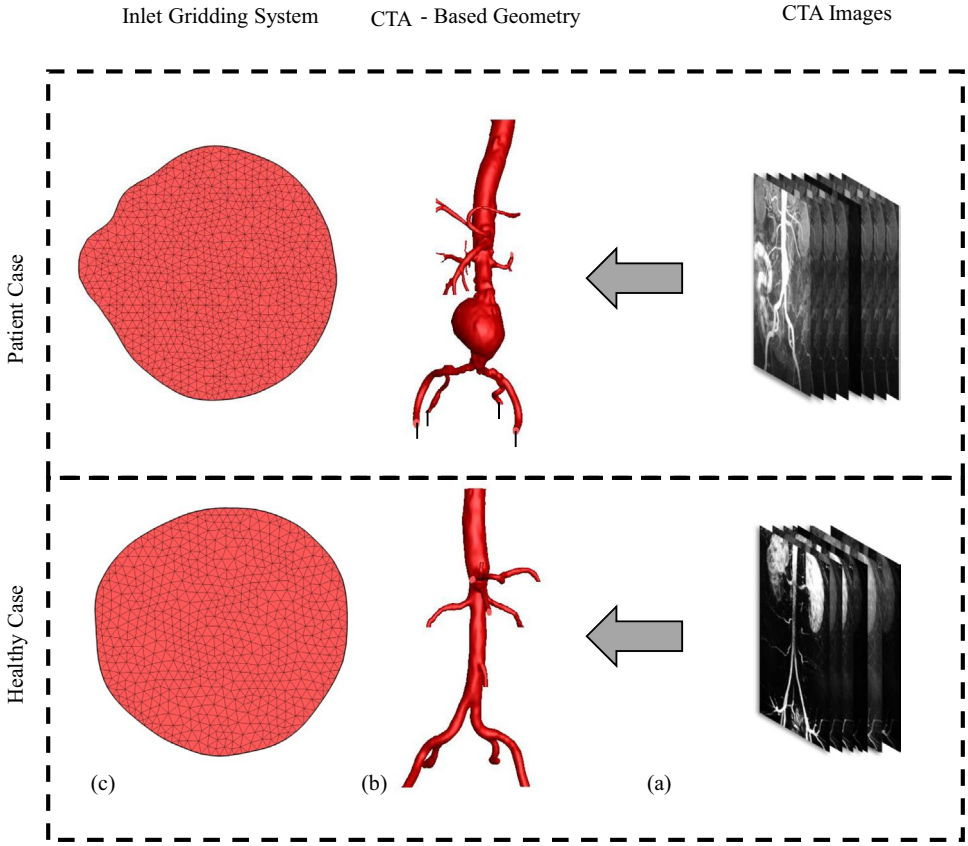

Fig. 10 **a** Presents the CTA images of the abdominal aorta aneurysm and healthy cases, **b** the computational domains (**b**), and **c** a magnified view of the computational mesh

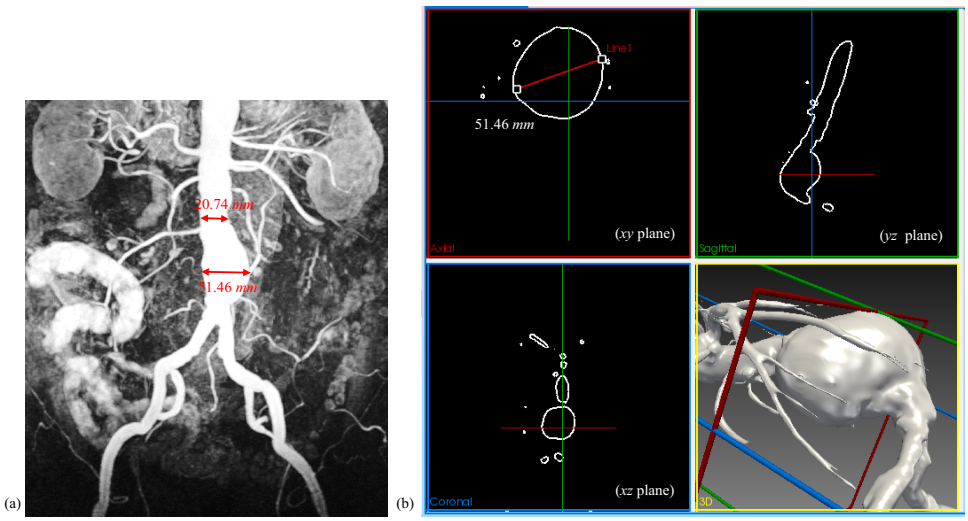

Fig. 11 **a** The CTA image for a patient-specific abdominal aortic aneurysm with a 148.12% area dilation and **b** showcases the size of the aneurysm constructed using SimVascular in the (*yz*), (*xy*), and (*xz*) planes

using SimVascular [35], as depicted in Fig. 10. The simulation process involves several steps. Firstly, the medical images depicting the examined part are carefully selected. Key points at the center of the artery and its main branches are identified and connected to create path lines. In the second step, the artery is segmented based on these points. In the third step, the 3D modelling of the CTA-based model is generated after the segmentation process using the modelling tool, as shown in Figs. 10b and 11. The aneurysm size is characterized by a dilation ratio of 2.48 compared to the inlet of the main vessel, as depicted in Fig. 11 which was the reason to use the range of d/D values from 1 to 2.6 with the benchmarks.

The setup for Phase II is similar to Phase I, with the difference being the use of transient simulation. In Phase II, the boundary conditions are obtained through ultrasonography of the patient, providing us with the velocity profile at the inlet and the pressure profile at the outlet, as depicted in Fig. 12 [25]. The velocity and pressure profiles are represented

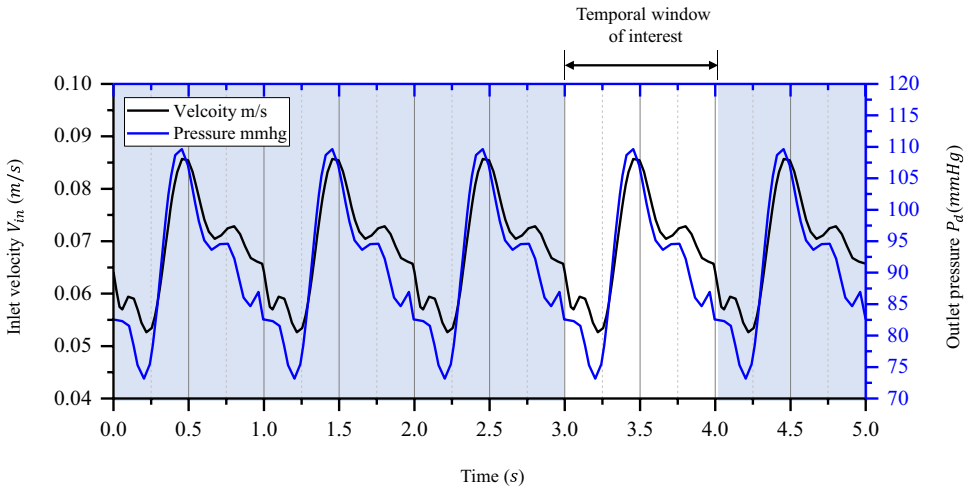

Fig. 12 The velocity profiles imposed on the artery inlet and the pressure profiles imposed on the artery outlets

as periodic transient table to be interpolated using the Fluent software at each time step. The simulation is done for 5 cardiac cycles with taking the results in the 4th one to make sure there is no numerical error due to the initialization.

3.2.1 The flow structure

The presence of aneurysm case has a significant impact on the flow behavior, particularly in terms of flow recirculation. In Fig. 13, a comparison of the flow streamlines between aneurysm and the healthy cases at different time periods of pulsations is depicted. The findings demonstrate that within the aneurysm zone, the magnitude of blood velocity is lower compared to the healthy case. This reduction is attributed to the increased cross-sectional area of the blood vessel caused by the presence of the aneurysm. In the case of a fusiform aneurysm, where the dilation extends around the entire circumference of the artery, the flow patterns can become highly intricate. The presence of the aneurysmal sac creates a region of disturbed flow, leading to the formation of recirculation zones where blood can flow backward or create eddies within the aneurysm. By investigating the flow behavior in the aneurysm case as shown in Figs. 14 and 15. During the early diastole phase, the velocity within the aneurysm experienced a significant reduction. Specifically, it decreased from a maximum value of 0.096 m/s to 0.011 m/s at the midpoint of the aneurysm. This reduction corresponds to approximately 8.727 times the velocity at the inlet, as depicted in Figs. 14 and 15b. The velocity streamlines observed in this case exhibited a predominantly unidirectional flow pattern within the core of aneurysm, with stagnant fluid regions surrounding the core, as shown in Fig. 15d. The presence of stagnation in these regions minimizes the interaction between the fluid and the aneurysm wall. The evenly distributed flow reduces the fluid-wall interactions with the outlet edges, thereby mitigating the risk of rupture and lowering the hemodynamic wall parameters. This outcome is desirable in terms of minimizing the likelihood of the aneurysm rupture. In the systolic phase, the maximum velocity within the aneurysm core experiences a reduction of 7.095 times compared to the maximum velocity observed at the inlet. Specifically, it decreases from 0.149 to 0.021 m/s, as illustrated in Figs. 14 and 15b. As we move radially towards the wall of the aneurysm, the velocity gradually decreases until it reaches 0 m/s, as depicted in Fig. 15c and d. The velocity streamlines within the aneurysm zone generally exhibit a predominantly unidirectional flow pattern, indicating a smooth and continuous flow. However, in the vicinity of the inlet, particularly on the side of aneurysm, the flow behavior deviates from this unidirectional pattern, as illustrated in Fig. 14. In this region, the flow may exhibit more complex and turbulent characteristics, possibly due to the presence of flow disturbances caused by the aneurysm. The appearance of recirculation flow can be attributed to the velocity difference between the inlet velocity and the blood velocity near the wall. This velocity difference gives rise to a local vortex near the inlet wall, which becomes more pronounced when there is a higher velocity disparity between the two streams. The high velocity at the outlets of the aneurysm enhances the interaction between the fluid and the edges, resulting in increased wall hemodynamics. This heightened interaction poses a risk for aneurysm rupture and is considered undesirable.

At the deceleration phase, there is a noticeable decrease in flow velocity through the aneurysm case. This sudden reduction in velocity creates fluid instabilities within the aneurysm, as depicted in Fig. 14. The velocity within the aneurysm core is reduced by a factor of 4 compared to the inlet velocity, as shown in Fig. 15b. However, the magnitude of velocity reduction during the late deceleration phase is relatively smaller compared to that observed during the early

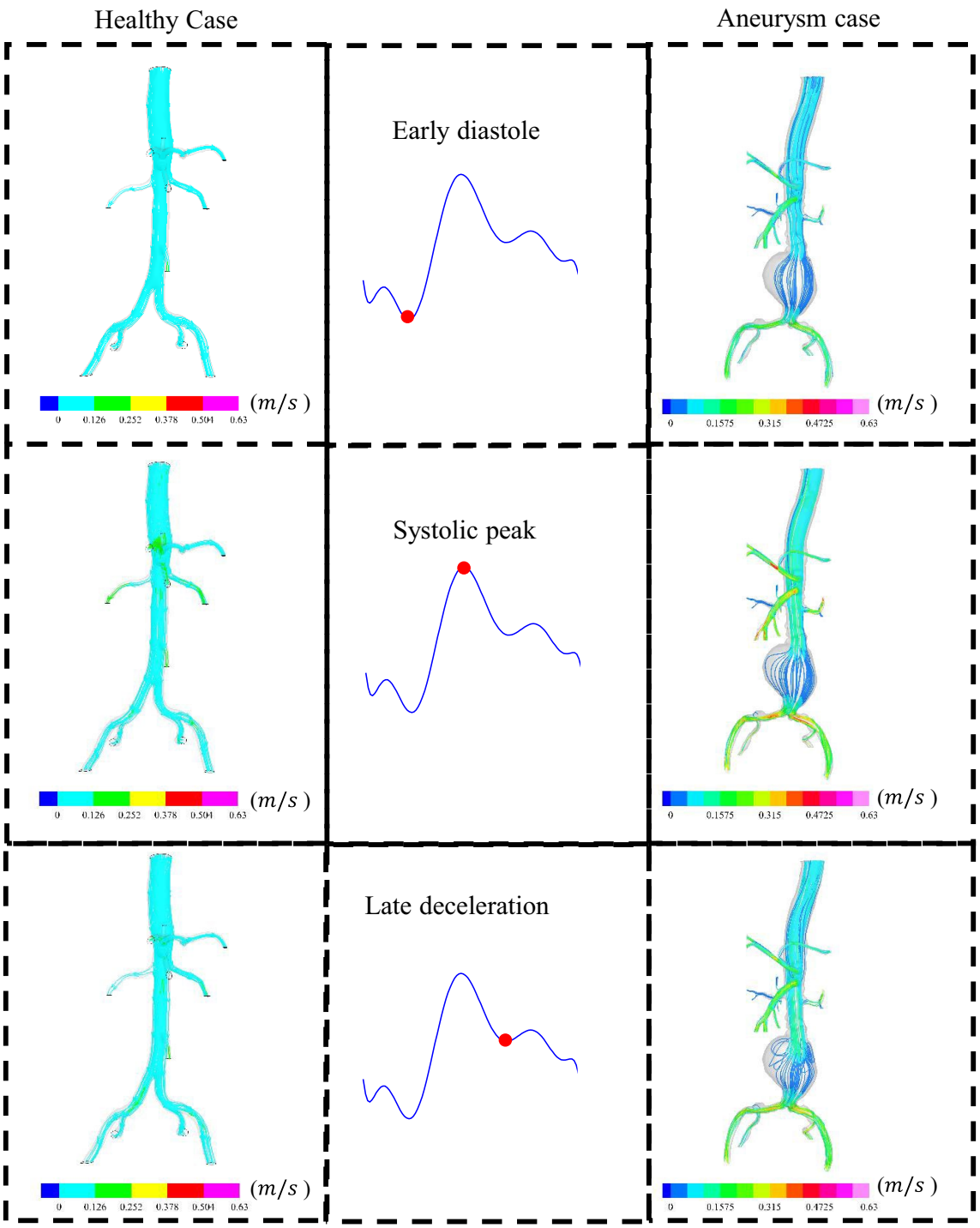

Fig. 13 The velocity streamlines for the aneurysm case and the healthy case at the early diastole, systolic peak, and late deceleration

diastole and systolic phases. The reason behind the fluid instabilities during late deceleration is the sudden decrease in velocity, which causes variations in the surrounding fluid and converts potential energy into kinetic energy. These kinetic energy fluctuations contribute to the development of fluid instabilities throughout the aneurysm, as illustrated in Fig. 15c and d. It is important to note that despite the smaller risk compared to the systolic phase, the high velocity at the outlets of the aneurysm still leads to undesirable wall hemodynamics features, posing a risk of rupture. While the risk of rupture is lower during the late deceleration phase compared to the systolic phase, it remains higher than during the early diastole phase.

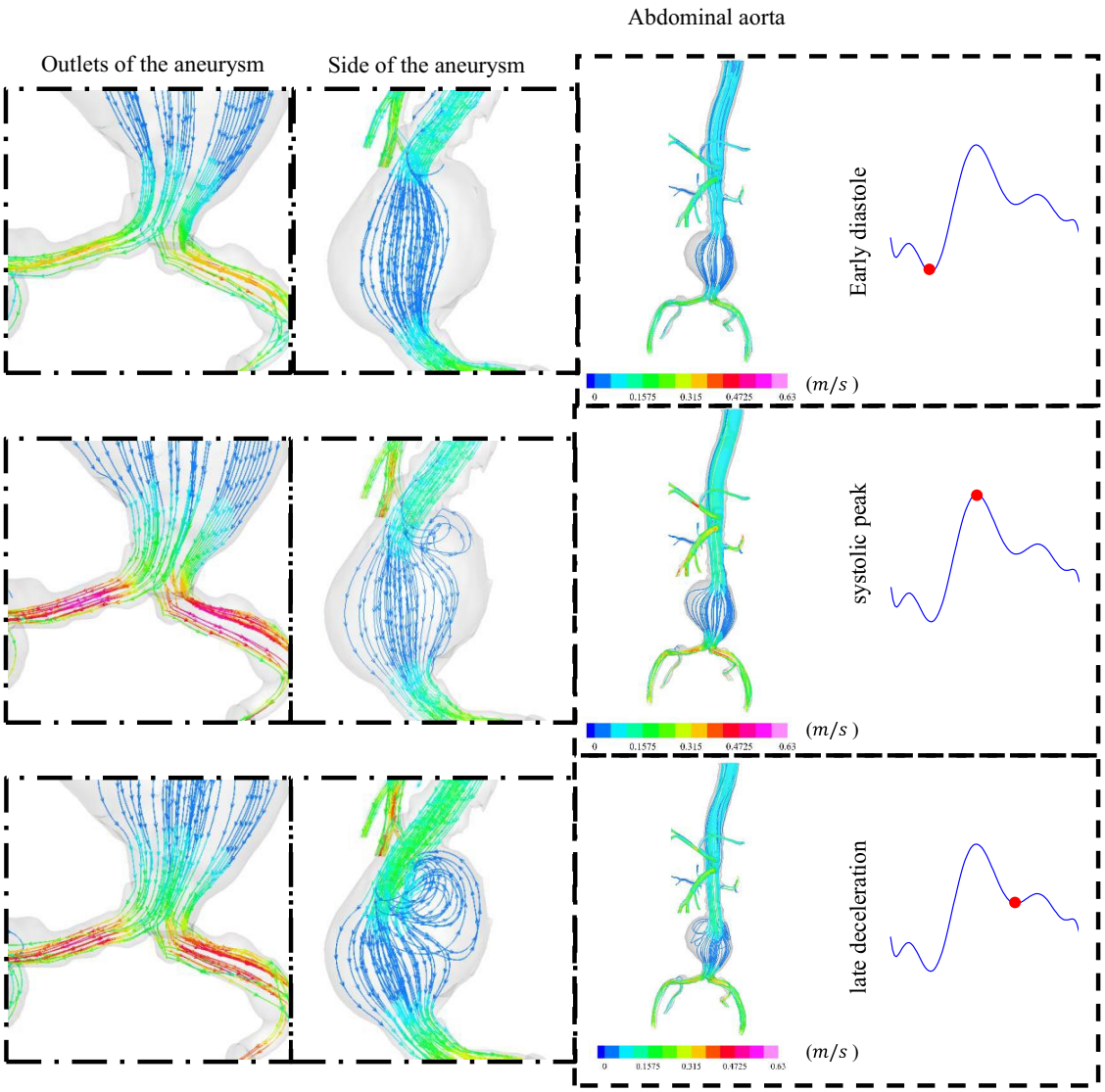

Fig. 14 The velocity streamlines for the aneurysm case, showing a zoomed-in view of the side of the aneurysm and the outlets

3.2.2 The wall shear stress

The wall shear stress experienced in cardiovascular vessels is influenced by multiple factors. These include blood flow velocity, vessel diameter, and geometry [36], blood viscosity, endothelial health, and vessel wall properties, as well as flow patterns and disturbances [2]. Higher blood flow velocities result in increased wall shear stress, while narrower vessels tend to have higher wall shear stress. The thickness or viscosity of the blood also affects wall shear stress, with higher viscosity leading to higher wall shear stress. The condition of the endothelial lining and the elasticity of the vessel wall can impact wall shear stress distribution. Disturbed flow patterns, such as recirculation zones or turbulent flow, can further affect the distribution of wall shear stress. The wall shear stress plays a critical role in regulating endothelial function, vascular remodeling, and overall vascular health, impacting processes like nitric oxide production, inflammation, thrombosis, and the development of atherosclerosis [37].

The presence of flow recirculation through the aneurysm has a significant impact on the wall shear stress. In Fig. 16, a comparison of the wall shear stress between the aneurysm case and the healthy case at different time periods of pulsations is depicted. The results reveal that the magnitude of wall shear stress within the aneurysm zone is lower compared to the healthy case, particularly at the outlets of the aneurysm. This decrease in wall shear stress can be attributed to the presence of flow instability, which leads to increased velocity values in those regions. Consequently,

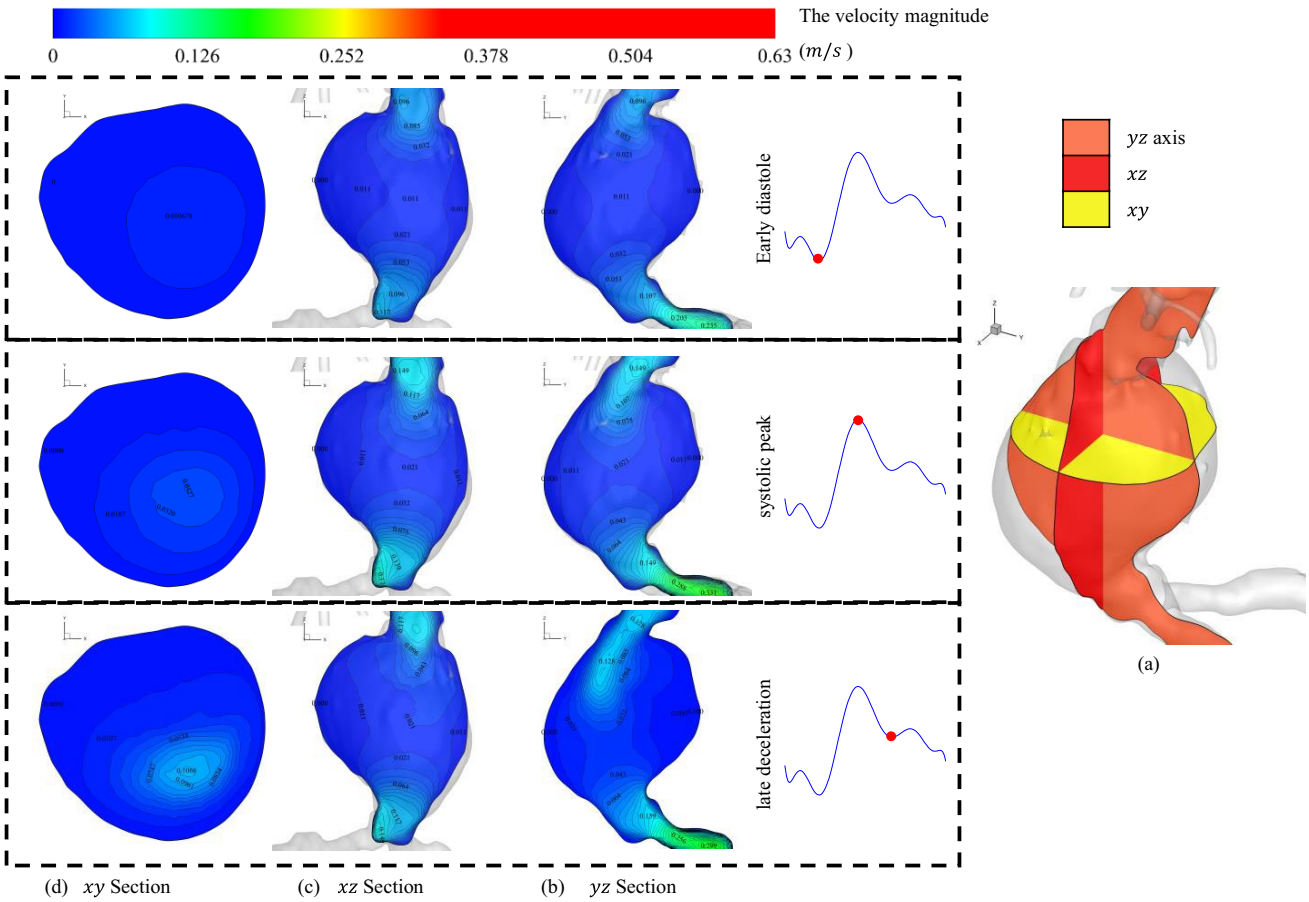

Fig. 15 Velocity Distribution Contours in **a** Three Cross-Sections of the aneurysm: **b** *yz* Plane, **c** *xz* Plane, and **d** *xy* Planets

the interaction between the high-velocity flow and the wall edges is intensified. As a result, the aneurysm case exhibits higher vulnerability to failure compared to the healthy case.

During the early diastole phase, the wall shear stress values are relatively lower compared to the systolic phase and late deceleration, as shown in Fig. 17. This is attributed to the lower velocity and the predominantly unidirectional flow along the artery during this phase. However, at the bifurcations of the artery, such as the first and second bifurcations, the wall shear stress values are significantly higher. This is due to the complex flow interaction at the bifurcation edges. At the second bifurcation inlet, there is a notable increase in wall shear stress as the fluid divides from the mainstream to the inlets. Additionally, at the outlets of the aneurysm, increase due to the interaction between the high-velocity flow and the outlet edges, as mentioned earlier. These findings highlight the variations in wall shear stress distribution throughout the cardiac cycle and the influence of fluid-wall interactions at bifurcations and the aneurysm outlets. During the systolic phase, the wall shear stress values reach their maximum due to the higher velocity of the flow, as depicted in Fig. 17. At the first and second bifurcations, the wall shear stress area at the bifurcation edges is larger compared to the early diastole phase, reaching up to 7 Pa. Particularly at the second bifurcation inlet, there is a significant increase in wall shear stress as the fluid divides from the mainstream to the inlets, especially in the upper region of the artery bending where the fluid reflects from the wall and continues within the main flow stream. Furthermore, at the outlets of the aneurysm, the wall shear stress values also reach their maximum, particularly at the bifurcation side edges, compared to other time periods. These observations highlight the impact of flow velocity and fluid behavior on the distribution of wall shear stress throughout the systolic phase, as well as the specific flow patterns and interactions occurring at bifurcation regions and aneurysm outlets.

During the deceleration phase, the fluid instabilities within the aneurysm have a significant impact on the wall shear stress, as illustrated in Fig. 17. Those instabilities (local vortex) lead to an increase in the value of the wall shear stress at the outlets of the aneurysm. The variation of wall shear stress is considered indicative of the potential location of aneurysm rupture. Research studies have indicated that regions characterized by wall shear stress high values variation are

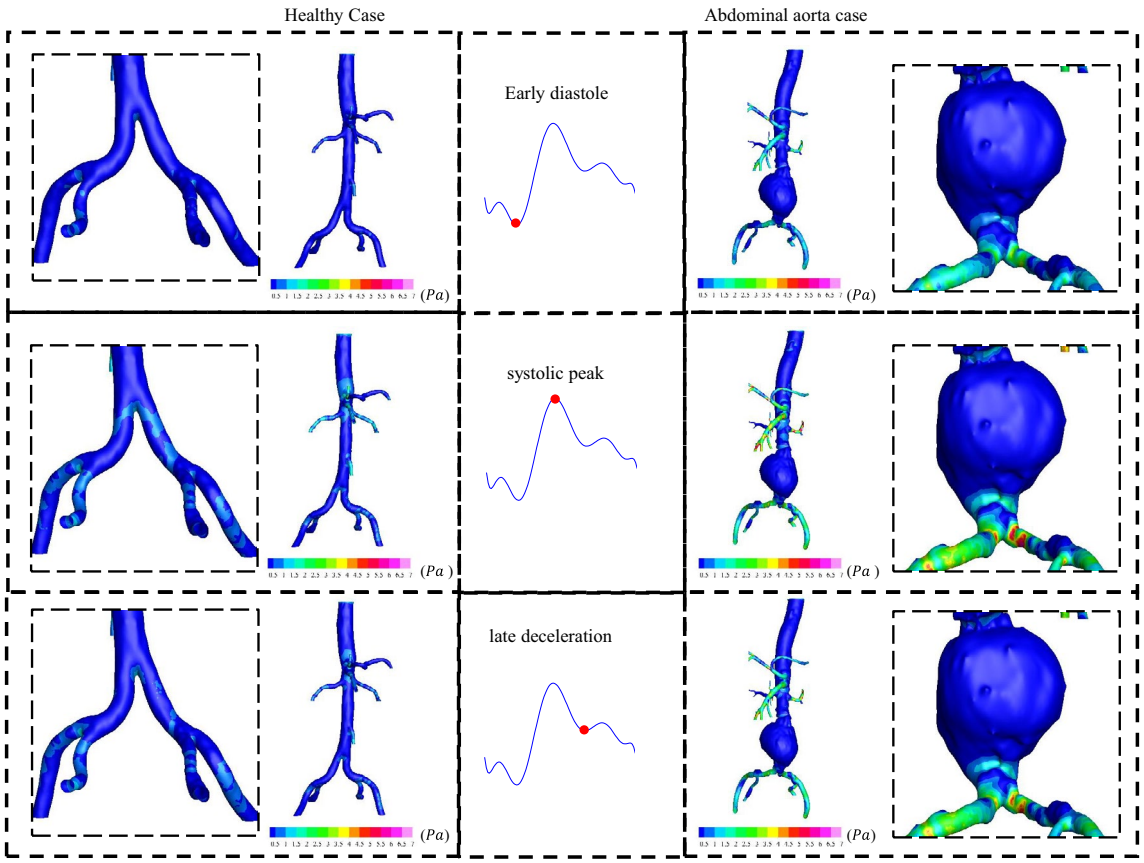

Fig. 16 The wall shear stress magnitude for aneurysm case and the healthy case at the early diastole, systolic peak, and late deceleration

more susceptible to rupture [38]. Specifically, the systolic phase poses a high risk of rupture due to the elevated levels of wall shear stress. Although the risk decreases during the deceleration phase compared to the systolic phase, it remains considerably higher than during the early diastole phase. These findings underscore the importance of monitoring and comprehending hemodynamic conditions, particularly the distribution of wall shear stress, to evaluate the risk of aneurysm rupture.

3.2.3 The pressure variation

The measurement of wall pressure in a fusiform aneurysm provides valuable information regarding its impact on hemodynamic parameters. It serves as an indicator for assessing factors such as blood flow patterns, wall shear stress, and vessel wall mechanics. By analyzing the distribution and magnitude of wall pressure, valuable insights can be gained regarding the stress exerted on the aneurysm's walls, which in turn affects the risk of rupture or further expansion. Additionally, the assessment of wall pressure helps identify flow disturbances, turbulence, and regions of high shear stress within the aneurysm. Overall, the examination of wall pressure aids in evaluating the hemodynamic conditions and their implications for the progression and management of a fusiform aneurysm. Throughout all phases, the wall pressure in the aneurysm case is consistently higher compared to the healthy case. This can be attributed to the presence of flow instabilities and disruptions in the aneurysm case, which are absent in the healthy case, as illustrated in Fig. 18. Specifically, during the early diastole phase, the aneurysm case demonstrates higher wall pressure compared to the healthy case. The average wall pressure in the aneurysm case is approximately 86.3 mmHg, whereas in the healthy case it is around 85.35 mmHg. The aneurysm case exhibits higher wall pressure, particularly at the bifurcations, compared to the healthy case. The healthy case shows a uniform distribution all over the wall at low pressure. At the systolic peak phase, the wall pressure in the aneurysm has an average value of approximately 104.76 mmHg, while the healthy case exhibits an average value of approximately 104.15 mmHg. The elevated wall pressure in the aneurysm case can be attributed to the flow instabilities present in the aneurysm, particularly at the bifurcations where the flow patterns are significantly

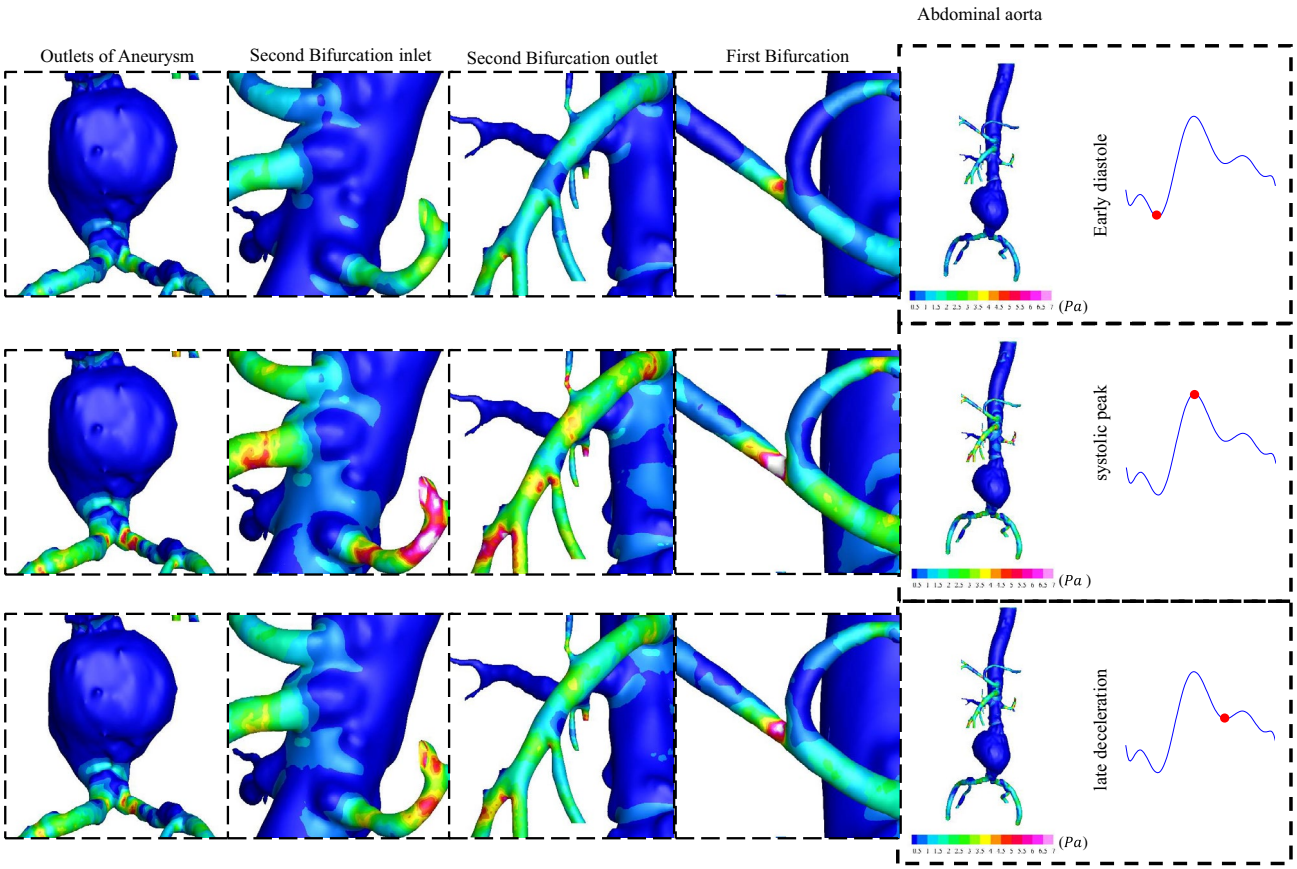

Fig. 17 The wall shear stress magnitude for the aneurysm case showing, zoomed-in views of the vascular bifurcation and the outlets of the aneurysm case

disturbed. In the deceleration phase, the wall pressure at the aneurysm is notably higher compared to the healthy case. The average wall pressure is approximately 95.5 mmHg for the aneurysm case, while in the healthy case, it is approximately 94.1 mmHg. This elevation in wall pressure within aneurysm case is particularly prominent at the bifurcations, where the pressure values are significantly higher compared to the healthy case. In contrast, the healthy case exhibits a more uniform distribution of wall pressure throughout the arterial system, indicating a more stable flow pattern and lower pressure fluctuations. The observed differences in wall pressure between aneurysm and the healthy case underscore the impact of the aneurysm on the hemodynamic conditions within the arterial system. The higher wall pressures for the aneurysm case, occurs at the bifurcations, suggest an increased risk of complications and highlight the importance of monitoring and managing aneurysmal conditions to mitigate the potential risks associated with elevated wall pressures.

4 Conclusions

Numerical simulations of the blood flow and wall shear stress distribution in vascular dilations, specifically on the abdominal aortic aneurysm are conducted. By employing advanced computational fluid dynamics simulations on both benchmark geometries and CTA-based abdominal aortic aneurysm models. This study has yielded significant insights into the flow characteristics and wall properties associated with these vascular conditions. One of the key findings of this study is the identification of distinct flow regimes within vascular dilations. We have observed various flow patterns, including stable flow, critical flow, transient flow, and stable flow with recirculation. These findings shed light on the complex dynamics occurring within vascular dilations, contributing to a deeper understanding of their behavior. The investigation of abdominal aortic aneurysm cases using the CTA-based models further expanded our knowledge of these specific vascular dilations. The simulations revealed a notable reduction in blood velocity

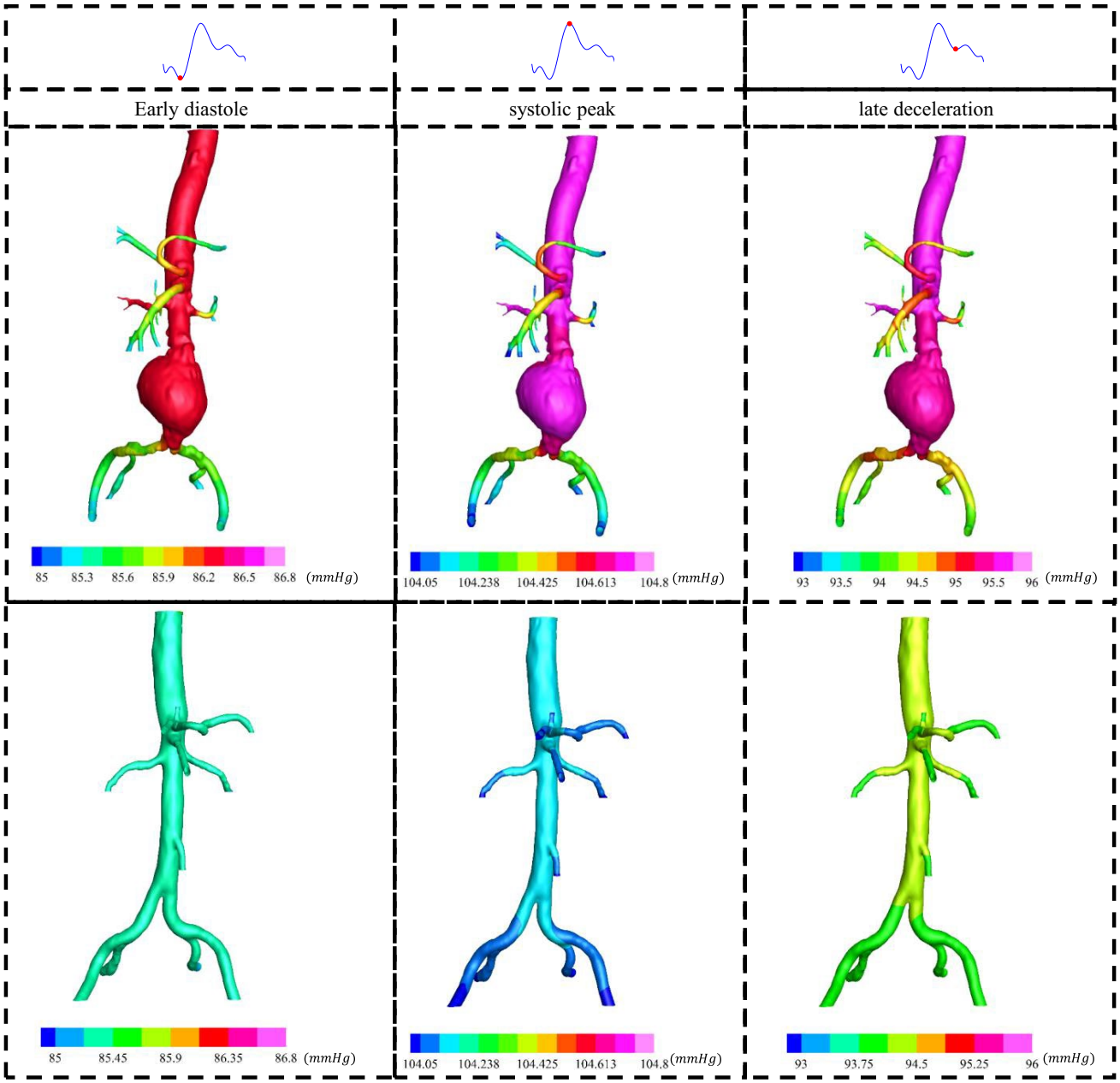

Fig. 18 Comparison of wall pressure between aneurysm and healthy case during early diastole, systolic peak, and late deceleration

within the aneurysm zone, indicating the altered flow dynamics present in these cases. Additionally, complex flow patterns were observed, with the presence of recirculation zones, which play a crucial role in the hemodynamics of abdominal aortic aneurysm.

The results demonstrated significant variations in wall shear stress distribution throughout the cardiac cycle, with higher values observed during systole and at bifurcations. In the stable recirculation flow regime, there is a sudden decrease in wall shear stress (Compared to Regime 2) at the end of the dilation due to the formation of a pillow, which reduces flow interaction with the bulge outlet edge. The aneurysm size is characterized by a dilation ratio of 2.48 compared to the inlet of the main vessel. Although the risk decreases during the deceleration phase compared to the systolic phase, it remains considerably higher than during the early diastole phase. These findings underscore the importance of monitoring and comprehending hemodynamic conditions, particularly the distribution of wall shear stress, to evaluate the risk of aneurysm rupture. In the deceleration phase, the wall pressure at the aneurysm is notably higher compared to the healthy case. The higher wall pressures for the aneurysm case, occurs at the bifurcations, suggest an increased

risk of complications and highlight the importance of monitoring and managing aneurysmal conditions to mitigate the potential risks associated with elevated wall pressures.

Acknowledgements Talaat Abdelhamid has been supported by grants of MIUR (PRIN_202232A8AN_003 and PRIN_P2022B38NR_002), funded by European Union - Next Generation EU.

Author contributions AGR: Conceptualization, methodology, investigation, data curation, Geometry preparation, numerical simulations, validation, visualization, and figure preparation. TA: Conceptualization, methodology, investigation, validation, draft revision, commenting, and supervision.

Data availability All data supporting the findings of this study are available within the paper and its Supplementary Information.

Declarations

Competing interests The authors declare no competing interests.

References

1. Luo L, Shiu W-S, Chen R, Cai X-C. A nonlinear elimination preconditioned inexact Newton method for blood flow problems in human artery with stenosis. J Comput Phys. 2019;399:108926. https://doi.org/10.1016/j.jcp.2019.108926.
2. Albadawi M, Abuouf Y, Elsagheer S, Ookawara S, Ahmed M. Predicting the onset of consequent stenotic regions in carotid arteries using computational fluid dynamics. Phys Fluids (1994). 2021;33:123106.
3. Lin K-Y, Shih T-C, Chou S-H, Chen Z-Y, Hsu C-H, Ho C-Y. Computational fluid dynamics with application of different theoretical flow models for the evaluation of coronary artery stenosis on CT angiography: comparison with invasive fractional flow reserve. Biomed Phys Eng Express. 2016;2(6):65011.
4. Xie X, Li Y, Xie S. Computation of hemodynamics in eccentric coronary stenosis: A morphological parametric study. Technol Health Care. 2018;26(2):229–38.
5. Karmonik C, Yen C, Grossman RG, Klucznik R, Benndorf G. Intra-aneurysmal flow patterns and wall shear stresses calculated with computational flow dynamics in an anterior communicating artery aneurysm depend on knowledge of patient-specific inflow rates. Acta Neurochir. 2009;151(5):479–85 (discussion 485).
6. Elhanafy A, Guaily A, Elsaid A. Numerical simulation of Oldroyd-B fluid with application to hemodynamics. Adv Mech Eng. 2019;11(5):168781401985284.
7. Piotr Reorowicz Z, Tyfa D, Obidowski K, Wiśniewski L, Stefańczyk K, Jóźwik. Michael Lee Levy, blood flow through the fusiform aneurysm treated with the Flow Diverter stent – Numerical investigations. Biocybernetics Biomedical Eng. 2022;42(1):375–90.
8. Rahma AG, Abdelhamid T. Hemodynamic and fluid flow analysis of a cerebral aneurysm: a CFD simulation. SN Appl Sci. 2023;5(2):62. https://doi.org/10.1007/s42452-023-05276-0.
9. Jing L, Fan J, Wang Y, Li H, Wang S, Yang X, et al. Morphologic and Hemodynamic Analysis in the patients with multiple intracranial aneurysms: ruptured versus unruptured. PLoS ONE. 2015;10(7):e0132494.
10. Li X, Simakov S, Liu Y, Liu T, Wang Y, Liang F. The influence of aortic valve disease on coronary hemodynamics: a computational model-based study. Bioeng (Basel). 2023;10(6):709.
11. Boutsianis E, Guala M, Olgac U, Wildermuth S, Hoyer K, Ventikos Y, Poulikakos D. CFD and PTV steady flow investigation in an anatomically accurate abdominal aortic aneurysm. J Biomech Eng. 2009;131(1):011008. https://doi.org/10.1115/1.3002886.
12. Ford MD, Nikolov HN, Milner JS, Lownie SP, Demont EM, Kalata W, Loth F, Holdsworth DW, Steinman DA. PIV-measured versus CFD-predicted flow dynamics in anatomically realistic cerebral aneurysm models. J Biomech Eng. 2008;130(2):021015. https://doi.org/10.1115/1.2900724.
13. Hoi Y, Woodward SH, Kim M, Taulbee DB, Meng H. Validation of CFD simulations of cerebral aneurysms with implication of geometric variations. J Biomech Eng. 2006;128(6):844–51.
14. Xiang J, Tutino VM, Snyder KV, Meng H. CFD: computational fluid dynamics or confounding factor dissemination? The role of hemodynamics in intracranial aneurysm rupture risk assessment. AJNR Am J Neuroradiol. 2014;35(10):1849–57.
15. Chen R, Wu B, Cheng Z, et al. A parallel non-nested two-level domain decomposition method for simulating blood flows in cerebral artery of stroke patient. Int J Numer Meth Biomed Eng. 2020;36:e3392.

16. Saalfeld S, Stahl J, Korte J, Miller Marsh LM, Preim B, Beuing O, Cherednychenko Y, Behme D, Berg P. Can Endovascular Treatment of Fusiform Intracranial Aneurysms Restore the Healthy Hemodynamic Environment?–A Virtual Pilot Study. Front Neurol. 2022;12:771694.
17. Sun Z, Chaichana T. Fenestrated stent graft repair of abdominal aortic aneurysm: hemodynamic analysis of the effect of fenestrated stents on the renal arteries. Korean J Radiol. 2010;11(1):95–106.
18. Wang H, Anzai H, Liu Y, Qiao A, Xie J, Ohta M. Hemodynamic-based evaluation on thrombosis risk of fusiform coronary artery aneurysms using computational fluid dynamic simulation method. Complexity. 2020;202:1–11.
19. Gregory Thompson B, BrownJr RD, Amin-Hanjani S, Broderick JP, Cockroft KM, Sander E, ConnollyJr GR, Duckwiler CC, Harris VJ, Howard S, Claiborne PM, Meyers A, Molyneux CS, Ogilvy AJ. Guidelines for the management of patients with unruptured intracranial aneurysms: A guideline for healthcare professionals from the American Heart Association/American stroke association. Stroke. 2015;46(8):2368–400.
20. Schievink WI. Intracranial aneurysms. N Engl J Med. 1997;336(1):28–40.
21. Johnston SC, Higashida RT, Barrow DL, Caplan LR, Dion JE, Hademenos G, Hopkins LN, Molyneux A, Rosenwasser RH, Vinuela F, Wilson CB, Committee on Cerebrovascular Imaging of the American Heart Association Council on Cardiovascular Radiology. Recommendations for the endovascular treatment of intracranial aneurysms: a statement for healthcare professionals from the Committee on Cerebrovascular Imaging of the American Heart Association Council on Cardiovascular Radiology. Stroke. 2002;33(10):2536–44.
22. Sakalihasan N, Limet R, Defawe OD. Abdominal aortic aneurysm. Lancet. 2005;365(9470):1577–89.
23. Salman HE, Ramazanli B, Yavuz MM, Yalcin HC. Biomechanical investigation of disturbed hemodynamics-induced tissue degeneration in abdominal aortic aneurysms using computational and experimental techniques. Front Bioeng Biotechnol. 2019;7:111.
24. Scotti CM, Shkolnik AD, Muluk SC, Finol EA. Fluid-structure interaction in abdominal aortic aneurysms: effects of asymmetry and wall thickness. Biomed Eng. 2005;4(1):64.
25. Rahma AG, Yousef K, Abdelhamid T. Blood flow CFD simulation on a cerebral artery of a stroke patient. SN Appl Sci. 2022;4(10):101.
26. Algabri YA, Rookkapan S, Chatpun S. Three-dimensional finite volume modelling of blood flow in simulated angular neck abdominal aortic aneurysm. IOP Conf Ser Mater Sci Eng. 2017;243:12003.
27. Petuchova A, Maknickas A. Computational analysis of aortic haemodynamics in the presence of ascending aortic aneurysm. Technol Heal Care. 2022;30(1):187–200.
28. Bhatti MM, Sait SM, Ellahi R. Magnetic nanoparticles for drug delivery through Tapered Stenosed artery with blood based non-newtonian fluid. Pharmaceuticals. 2022;15:1352.
29. Shaimaa F, Ramadan F, Mekheimer KS, Bhatti MM, Moawad AMA. Phan-thien-tanner nanofluid flow with gold nanoparticles through a stenotic electrokinetic aorta: A study on the cancer treatment. Heat Transf Res. 2021;52(16,2021):87–99.
30. Versteeg HK, Malalasekera W. An introduction to computational fluid dynamics: the finite volume method. 2nd ed. Harlow, England SE: Pearson Education Ltd; 2007.
31. Albadawi M, Abuouf Y, Elsagheer S, Sekiguchi H, Ookawara S, Ahmed M. Influence of rigid-elastic artery wall of carotid and coronary stenosis on hemodynamics. Bioeng. 2022;9(11):708.
32. Souza MS, et al. Fluid flow and structural numerical analysis of a cerebral aneurysm model. Fluids. 2022;7(3):100.
33. Akbar NS, Nadeem S. Carreau fluid model for blood flow through a tapered artery with a stenosis. Ain Shams Eng J. 2014;5(4):1307–16.
34. Abuouf Y, AlBadawi M, Ookawara S, Ahmed M. Effect of guidewire insertion in fractional flow reserve procedure for real geometry using computational fluid dynamics. Biomed Eng Online. 2021;20(1):95. https://doi.org/10.1186/s12938-021-00935-y.
35. Updegrove A, Wilson NM, Merkow J, Lan H, Marsden AL, Shadden SC. SimVascular: an Open Source Pipeline for Cardiovascular Simulation. Ann Biomed Eng. 2017;45(3):525–41. https://doi.org/10.1007/s10439-016-1762-8.
36. Rahma AG, Abdelhamid T. Assessing the effects of stenosis and aneurysms on hemodynamic parameters: A numerical investigation. Int Conf Electr Eng. 2023;23:34.
37. Dhawan SS, Avati Nanjundappa RP, Branch JR, Taylor WR, Quyyumi AA, Jo H, McDaniel MC, Suo J, Giddens D, Samady H. Shear stress and plaque development. Expert Rev Cardiovasc Ther. 2010;8(4):545–56.
38. Kenji Yoshiki K, Misaki I, Nambu I, Fukui M, Mohri N, Uchiyama. Mitsutoshi Nakada; Intraoperative Rupture of Unruptured Cerebral Aneurysm during Craniotomy: A Case Report. Case Rep Neurol. 2018;9(3):261–6.